





Publication Year	2018
Acceptance in OA@INAF	2020-10-13T09:23:14Z
Title	Dark halo structure in the Carina dwarf spheroidal galaxy: joint analysis of multiple stellar components
Authors	Hayashi, Kohei; FABRIZIO, Michele; Aokas, Ewa L.; B Matteo; et al.
DOI	10.1093/mnras/sty2296
Handle	http://hdl.handle.net/20.500.12386/27751
Journal	MONTHLY NOTICES OF THE ROYAL ASTRONOMICAL SOCIETY
Number	481

Dark halo structure in the Carina dwarf spheroidal galaxy: joint analysis of multiple stellar components

Kohei Hayashi ^{1,2★} Michele Fabrizio^{3,4} Ewa L. Łokas⁵ Giuseppe Bono^{3,6}
Matteo Monelli ^{7,8} Massimo Dall’Ora⁹ and Peter B. Stetson¹⁰

¹National Astronomical Observatory of Japan, 2-21-1 Osawa, Mitaka, Tokyo 181-8588, Japan

²Institute for Cosmic Ray Research (ICRR), The University of Tokyo, Chiba 277-8583, Japan

³INAF - Osservatorio Astronomico di Roma, Via di Frascati 33, I-00078 Monte Porzio Catone (Roma), Italy

⁴Space Science Data Center - ASI, Via del Politecnico SNC, I-00133 Roma, Italy

⁵Nicolaus Copernicus Astronomical Center, Polish Academy of Sciences, Bartycka 18, PL-00-716 Warsaw, Poland

⁶Dipartimento di Fisica, Università di Roma “Tor Vergata”, Via della Ricerca Scientifica 1, I-00133 Roma, Italy

⁷Instituto de Astrofísica de Canarias, Calle Via Lactea, E-38205 La Laguna, Tenerife, Spain

⁸Universidad de La Laguna, Dpto. Astrofísica, E-38206 La Laguna, Tenerife, Spain

⁹INAF-Osservatorio Astronomico di Capodimonte, Salita Moiariello 16, I-80131 Napoli, Italy

¹⁰Dominion Astrophysical Observatory, NRC-Herzberg, National Research Council, 5071 West Saanich Road, Victoria, BC V9E 2E7, Canada

Accepted 2018 August 17. Received 2018 July 20; in original form 2018 April 4

ABSTRACT

Photometric and spectroscopic observations of the Carina dSph revealed that this galaxy contains two dominant stellar populations of different age and kinematics. The coexistence of multiple populations provides new constraints on the dark halo structure of the galaxy, because different populations should be in equilibrium in the same dark matter potential well. We develop non-spherical dynamical models including such multiple stellar components and attempt to constrain the properties of the non-spherical dark halo of Carina. We find that Carina probably has a larger and denser dark halo than found in previous works and a less cuspy inner dark matter density profile, even though the uncertainties of dark halo parameters are still large due to small volume of data sample. Using our fitting results, we evaluate astrophysical factors for dark matter annihilation and decay and find that Carina should be one of the most promising detectable targets among classical dSph galaxies. We also calculate stellar velocity anisotropy profiles for both stellar populations and find that they are both radially anisotropic in the inner regions, while in the outer regions the older population becomes more tangentially biased than the intermediate ones. This is consistent with the anisotropy predicted from tidal effects on the dynamical structure of a satellite galaxy and thereby can be considered as kinematic evidence for the tidal evolution of Carina.

Key words: galaxies: dwarf – galaxies: kinematics and dynamics – dark matter – galaxies: Carina.

1 INTRODUCTION

Dwarf spheroidal (dSph) galaxies in the Local Group are an excellent test-bed for understanding the fundamental properties of dark matter and galaxy formation processes involving this non-baryonic matter. In the area of particle physics, these satellites have drawn special attention as ideal sites for obtaining limits on particle candidates of TeV-scaled dark matter (Lake 1990; Walker 2013; Geringer-Sameth, Koushiappas & Walker 2015; Hayashi et al. 2016). This is because these galaxies have high dynamical mass-to-light ratios

($M/L \sim 10\text{--}1000$), that is, they are the most dark matter-dominated systems (McConnachie 2012, and the references therein). Moreover, these galaxies are sufficiently close to measure line-of-sight velocities for their resolved member stars by high-resolution spectroscopy, and this kinematic information enables us to study structural properties of dark matter haloes in less-massive galaxies in detail.

Using these high-quality data, the studies of dSphs have suggested some intriguing properties of dark haloes in dSphs; some of them may have cored or at least shallower cuspy dark matter profiles (Gilmore et al. 2007; Battaglia et al. 2008; Walker & Peñarrubia 2011), are most likely to have non-spherical dark halo (Hayashi & Chiba 2012, 2015b), and their dark haloes show some universal

* E-mail: kohei.hayashi@ipmu.jp

properties (Salucci & Burkert 2000; Strigari et al. 2008; Boyarsky et al. 2010; Salucci et al. 2012; Hayashi & Chiba 2015a; Kormendy & Freeman 2016; Hayashi et al. 2017). In particular, cored dark halo profiles in dSphs are in disagreement with those predicted from dark matter simulations based on cold dark matter (CDM) models, which showed that the density profile of a dark halo of any mass is well fit by a Navarro–Frenk–White profile (hereafter NFW; Navarro, Frenk & White 1996, 1997). This issue is the so-called ‘core-cusp’ problem, and it is yet a matter of ongoing debate. In order to solve or alleviate the above issue, a possible solution has been proposed that relies on a transformation mechanism from cusped to cored central density. Recent high-resolution cosmological N -body and hydrodynamical simulations in the context of CDM models have shown that inner dark halo profiles at dwarf-galaxy mass scale could be transformed to cored ones due to the effects of energy feedback from star formation activity such as radiation energy from massive stars, stellar winds, and supernova explosions (Governato et al. 2012; Di Cintio et al. 2014a,b; Madau, Shen & Governato 2014; Ogiya & Mori 2014; Oñorbe et al. 2015).

Another possible solution is to replace CDM with alternative dark matter models such as warm dark matter or self-interacting dark matter models, which can form cored and less-dense central dark matter profiles on less massive scales without baryonic effects (Spergel & Steinhardt 2000; Vogelsberger, Zavala & Loeb 2012; Anderhalden et al. 2013; Elbert et al. 2015; Bozek et al. 2016). However, because of the dependence on the observational and theoretical uncertainties, it is difficult to discriminate between these two different transformation mechanisms on the basis of observational facts, hence the core-cusp problem still persists.

On the other hand, current kinematic studies of dSphs are unable to determine precisely dark halo structures in these galaxies because of the presence of degeneracy in mass models, which stems from the fact that only projected kinematic information is available and dynamical models are incomplete. For example, kinematic studies typically treat dSph galaxies as spherically symmetric systems with constant-velocity anisotropy along the radii. However, in such models, there is a degeneracy between the velocity anisotropy of stars and dark matter density profiles (Evans, An & Walker 2009; Walker et al. 2009). Even for axisymmetric mass models, similar degeneracy between stellar velocity anisotropy and the global shape of dark halo exists (Cappellari 2008; Hayashi & Chiba 2015b; Hayashi et al. 2016). The studies of dark matter in dSph galaxies have been hampered by these degeneracies. In order to disentangle this ambiguity, at least in part, so far unknown kinematical information on dSphs and/or more general dynamical models are required. Recently, owing to the outstanding quality of *Gaia* (Gaia Collaboration 2016, 2018a,b), the precision proper motions of nearby bright stars are available. Using the proper motions of 15 member stars in Sculptor dSph based on data from the *Gaia* and the *Hubble Space Telescope*, Massari et al. (2018) measured the internal motions of the stars and obtained the limit on the velocity anisotropy. Although there exists a large uncertainty on this anisotropy with the paucity of data sample, a number of proper-motion data from the *Gaia* and future astrometry observations (e.g. Wide Field Infrared Survey Telescope, Spergel et al. 2015), NFIRAOS at Thirty Meter Telescope (Herriot et al. 2014), and MICADO/MAORY at Extremely Large Telescope (Fiorentino et al. 2017 and so on) will enable us to tackle the issues of the degeneracies head-on.

Recent spectroscopic observations found that some classical dSphs (Sculptor, Fornax, and Sextans) exhibit multiple chemo-dynamical subpopulations (Tolstoy et al. 2004; Battaglia et al. 2006, 2008, 2011). For instance, Battaglia et al. (2008) found that in the

Sculptor dSph metal-rich stars are centrally concentrated and have colder kinematics with the line-of-sight velocity dispersion decreasing with radius, whereas metal-poor ones are more extended and have hotter kinematics and an almost constant dispersion profile. From the perspective of dynamical modelling, the presence of these intriguing chemo-dynamical stellar properties provides new constraints on the dark halo structure of dSphs. This is because these kinematically different populations should settle in the same dark matter potential well, and thus the coexistence of multiple populations enhances our ability to infer the inner structure of the dark matter halo (Battaglia et al. 2008; Walker & Peñarrubia 2011; Agnello & Evans 2012; Amorisco & Evans 2012; Amorisco, Agnello & Evans 2013; Breddels & Helmi 2014; Strigari, Frenk & White 2017)

Battaglia et al. (2008) were the first to attempt to set constraints on the inner slope of dark matter profile in the Sculptor dSph using multiple stellar components. Using spherical Jeans models, they found that cored dark halo models provide a better fit than NFW models, which however could not be ruled out. Later, Walker & Peñarrubia (2011) have separated multiple stellar components using a combined likelihood function for spatial, metallicity, and velocity distributions, and then constrained the dark matter slopes of the Sculptor and Fornax dSphs through the mass slope using metal-rich and metal-poor populations and assuming a spherical stellar system. They concluded that both Fornax and especially Sculptor have central cores, ruling out the NFW profile at high statistical significance. However, if a dSph is not spherical, assuming sphericity in their method may lead to a strong bias and the inferred slope turns out to depend on the line of sight (Kowalczyk et al. 2013; Genina et al. 2018). In contrast, adopting a separable model for the distribution function (DF) of an equilibrium spherical system Strigari et al. (2017) showed that the two chemo-dynamical subpopulations in Sculptor are consistent with an NFW profile. Furthermore, Breddels & Helmi (2014) applied Schwarzschild methods to two stellar subpopulations in Sculptor and concluded that the fitting results with the NFW model are indistinguishable from those with a cored one. Therefore, the remarkable debate as to whether the central regions of haloes in dSphs are cored or cusped is still ongoing.

All these studies assumed, however, that the stellar and dark components are spherical, even though we know both from observations and theoretical predictions that these components should be actually non-spherical. Zhu et al. (2016) applied the discrete Jeans anisotropic multiple Gaussian expansion model (Watkins et al. 2013) to the chemo-dynamical data of the Sculptor dSph assuming that stellar distributions are free to be axisymmetric but a dark matter halo is spherical. On the other hand, Hayashi & Chiba (2015b) have constructed axisymmetric mass models based on axisymmetric Jeans equations, including stellar velocity anisotropy and applied these models to line-of-sight velocity dispersion profiles of the luminous dSphs associated with the Milky Way and Andromeda. Hayashi et al. (2016, hereafter H16) applied the generalized axisymmetric mass models developed by Hayashi & Chiba (2015b) to the most recent kinematic data for the ultra faint dwarf galaxies as well as classical dSphs, but they performed an unbinned analysis for the comparison between data and models, unlike Hayashi & Chiba (2015b). However, these non-spherical mass models have not yet been applied to two-component systems in any dSphs.

In this paper, following the axisymmetric mass models developed by H16 and using an unbinned analysis, we develop the multiple stellar component mass models to obtain stronger limits on dark halo structures in dSphs and apply these models to the line-of-sight velocity data of two different age populations in the Carina dSph. As

a result of a long-term photometric and spectroscopic observation project for Carina (Carina Project: Dall’Ora et al. 2003; Monelli et al. 2003; Fabrizio et al. 2011, 2012; Coppola et al. 2013; Monelli et al. 2014; Fabrizio et al. 2015, 2016), it has been shown that the stars in this galaxy can be separated into an intermediate-age and an old-age population using the colour–magnitude diagram derived from these photometric data. The spectroscopic data for a fraction of these stars were then obtained using Very Large Telescope (as described in next section in more detail). Therefore, in this work we focus on the constraints on the dark halo structure in Carina that can be obtained using the mass models we developed and recent photometric and spectroscopic data for the two stellar populations. Moreover, the important point in this work is that we attempt for the first time to set constraints on a non-spherical dark halo of Carina using the data for its two stellar subpopulations.

The paper is organized as follows. In Section 2, we describe the photometric and spectroscopic data for Carina dSph. In Section 3, we explain axisymmetric models for density profiles of stellar and dark halo components based on an axisymmetric Jeans analysis. In Section 4, we introduce the method of fitting the data and the joint likelihood function we adopted. In Section 5, we present the results of the fitting and compare these with the ones from the single likelihood function analysis. In Section 6, we discuss astrophysics factors for dark matter annihilation and decay and the stellar velocity anisotropy profile for each population. Finally, conclusions are presented in Section 7.

2 INTERMEDIATE- AND OLD-AGE STELLAR POPULATIONS OF CARINA

The Carina dSph galaxy is centred at $(\alpha_{2000}, \delta_{2000}) = (06^{\text{h}}41^{\text{m}}36.7^{\text{s}}, -50^{\circ}57'58'')$ with a position angle measured North through East of 65° , and is located at a heliocentric distance, $D_{\odot} = 106 \pm 6$ kpc (Irwin & Hatzidimitriou 1995; McConnachie 2012). In this section, we briefly introduce the photometric and kinematic data of two stellar components in Carina dSph (Bono et al. 2010; Monelli et al. 2014; Fabrizio et al. 2016, for more details)

In this work, we use the photometric data from three different telescopes, i.e. the CTIO 1.5 m telescope, the CTIO 4 m Blanco telescope, and the ESO/MPG 2.2 m telescope (Bono et al. 2010) and the spectroscopic data from high- and medium-resolution spectrographs mounted at the Very Large Telescope (Fabrizio et al. 2016). Based on photometric $V - c_{U,B,I}$ diagram, i.e. V-band magnitude versus the new photometric colour index, $c_{U,B,I} = (U - B) - (B - I)$, for the individual stars (Monelli et al. 2013), the member stars of Carina can be separated into the intermediate-age (red clump and subgiant stars) and the old-age (horizontal branch and subgiant stars) stellar populations. This is possible because $c_{U,B,I}$ is strongly sensitive to stellar metallicity, especially helium and light-element content (Bono et al. 2010).¹ Fig. 1 shows the V versus $B - I$ (left-hand panel) and V versus $c_{U,B,I}$ diagram (right-hand panel) for the photometric observations of Carina. It is clear from the right-hand panel of Fig. 1 that the Carina dSph clearly has two main sub-populations.

On the other hand, performing new observations and reducing the data for the stellar spectra, and collecting other currently available

data for Carina, Fabrizio et al. (2016) performed a detailed analysis of velocity distributions of 1096 intermediate-age and 293 old population stars. This analysis revealed that while the intermediate-age stellar component shows a weak rotational pattern around the minor axis, the old one has a larger line-of-sight velocity dispersion and is more extended towards the outer region. They also looked into stellar distributions of both populations and found that the intermediate-age stars in this galaxy are centrally concentrated, whereas the old ones are more extended in the outer region. These photometric and kinematic features are roughly in agreement with those of similar multiple populations in Sculptor, Sextans, and Fornax (Battaglia et al. 2008, 2011; Amorisco & Evans 2012). Thus, these features of multiple stellar populations in the luminous dSphs could be general and universal.

In what follows, using in total 6633 (3757 intermediate and 2876 old) photometric and 1389 (1096 intermediate and 293 old) spectroscopic measurements, which is spectroscopic data volume almost twice larger than that of previous works, we investigate structural properties of stellar distributions for each stellar population and the dark matter distribution in the Carina dSph.

3 TWO-COMPONENT MASS MODELLING FOR CARINA

3.1 Luminous components

In order to solve the second-order Jeans equations and set constraints on dark halo properties of the Carina dSph, we should first obtain the structural properties of stellar populations. Here, we present briefly the procedure to estimate their stellar profiles.

In this work, we assume that the member stars on the sky plane are distributed by the Sérsic profile (Sérsic 1968),

$$I_{\text{Ser}}(R') = I_{S,0} \exp \left[- \left(\frac{R'}{R_s} \right)^{\frac{1}{m}} \right], \quad (1)$$

by the Plummer profile (Plummer 1911)

$$I_{\text{Plm}}(R') = I_{P,0} \frac{R_p^2}{(R_p^2 + R'^2)^2}, \quad (2)$$

and by the exponential profile,

$$I_{\text{Exp}}(R') = I_{E,0} \exp \left\{ - \left(\frac{R'}{R_e} \right) \right\}, \quad (3)$$

where $I_{(S,P,E),0}$ are the central surface densities, and $R_{(s,p,e)}$ denote the scale radii of each stellar distribution. m in Sérsic profile is the Sérsic index, which measures the curvature of the stellar profile, and $m = 1$ corresponds to the exponential profile. The projected elliptical radius, R' , related to projected sky coordinates (α, δ) , is given by

$$R'^2 = (X \cos \theta - Y \sin \theta)^2 + \left[\frac{1}{1 - \epsilon} (X \sin \theta + Y \cos \theta) \right]^2, \quad (4)$$

$$X = (\alpha - \alpha_0) \cos(\delta_0), \quad Y_i = \delta - \delta_0, \quad (5)$$

where (α_0, δ_0) is the centroid of the system, θ is the position angle of the major axis, defined East of North on the sky, and ϵ is an ellipticity defined as $\epsilon = 1 - q'$, with $q' = b/a$ being the projected minor-to-major axial ratio of the galaxy.

In order to estimate the stellar structural parameters of Carina, we compare the radial profiles estimated from the photometric data with those of the modelled profiles with some free parameters. First, adopting the standard binning approach, we estimate the projected

¹Since there are two well-defined star formation events characterizing Carina stellar populations, this age separation is plausible, even though $c_{U,B,I}$ is mainly sensitive to chemical compositions. Namely, the more metal-poor population would be intrinsically older in a stellar system.

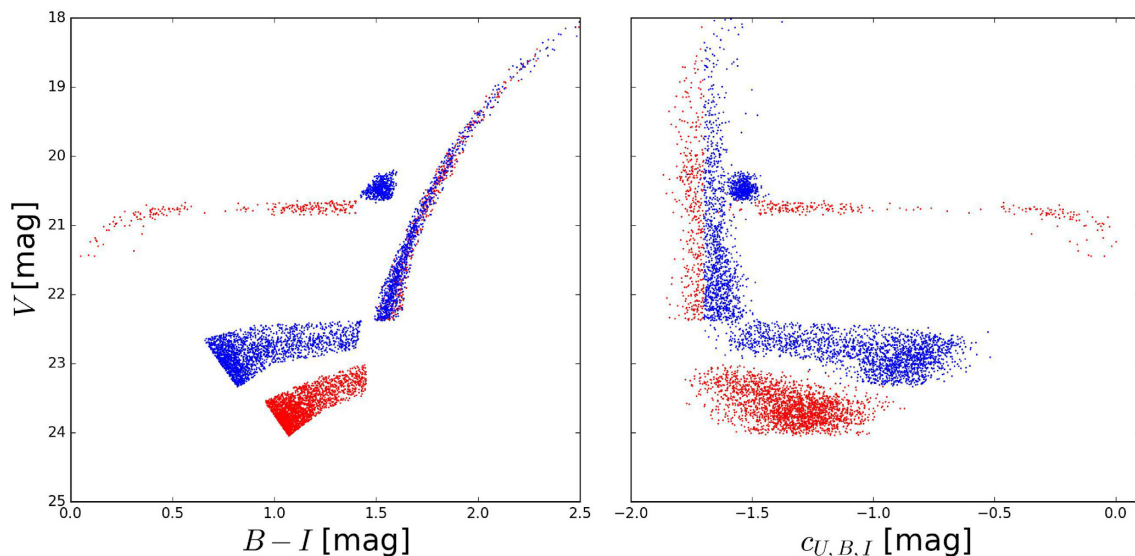


Figure 1. Left-hand panel – Photometric selection of intermediate-age (blue) and old (red) candidate Carina stars based on the V versus $(B - I)$ CMD. The former includes the red clump stars and bright subgiant branch stars, while the latter one includes horizontal branch stars and faint subgiant branch stars. Right-hand panel – Same as the left-hand panel, but in the V versus $c_{U,B,I}$ diagram. The intermediate and old-age candidates selected in the left-hand panel are also plotted with blue and red symbols.

radial profiles for each population. We set the radial bins so that a nearly equal number of stars is contained in each bin, and then derive the surface density profiles using the number of stars contained in each bin. The points with error bars in Fig. 2 show the binned profiles estimated from the photometric data. The error bars are assumed to be the Poisson errors. To obtain the stellar structural parameters of the assumed models by comparing with observational data, we employ a simple χ^2 test,

$$\chi^2 = \sum_i^{N_{\text{bins}}} \frac{[I_i^{\text{obs}} - I_i^{\text{model}}(O)]^2}{\varepsilon_i^2}, \quad (6)$$

where N_{bins} is the number of bins, I^{obs} is the measured stellar surface density, I^{model} is the modelled density at the same distance from the centre of the system, and ε is the error on I^{obs} . O denotes the structural parameters of the assumed models, that is, $I_{(S,P,E),0}$, $R_{(s,p,e)}$, ε , and the Sérsic index m . We employ the reduced χ^2 statistics that takes the value of χ^2 divided by the number of degrees of freedom, usually given by $N_{\text{bins}} - N_{\text{parameters}}$, where $N_{\text{parameters}}$ is the number of parameters.

The fitting results for the structural parameters are tabulated in Table 1, and Fig. 2 shows the radial profiles using the best-fitting values of the parameters. Although we estimate also the best-fitting value of the parameter $I_{(S,P,E),0}$, it is not an important parameter because it should vanish when we calculate Jeans equations, as discussed below. Thus, this parameter is not tabulated in Table 1. According to these results, we confirm that the intermediate-age subcomponent is more centrally concentrated than the old one, which is in agreement with Monelli et al. (2003, see also Fabrizio et al. 2016), and find that the Sérsic profile is the best-fitting model in each population among the three stellar profile models we considered. Thus, we adopt the Sérsic profile as the fiducial stellar distribution of each population and incorporate it into Jeans equations.

The three-dimensional stellar density $\nu(r_*)$ is obtained from the surface density $I_{\text{Ser}}(R')$ by deprojection through the Abel transform. In the case of $m = 1$, we can obtain it in the analytical form, $\nu(r_*, m = 1) = S_0 K_0(r_*/R_s)/(\pi R_s)$, where $K_0(x)$ is the modified

Bessel function of the second kind. On the other hand, in the case of $0.5 \leq m \leq 10$, there is an excellent approximation for $\nu(r_*)$ derived by Lima Neto, Gerbal & Márquez (1999):

$$\nu(r_*) = \nu_0 \left(\frac{r_*}{R_s}\right)^{-p} \exp\left[-\left(\frac{r_*}{R_s}\right)^{1/m}\right], \quad (7)$$

where

$$\nu_0 = \frac{I_0 \Gamma(2m)}{2R_s \Gamma[(3-p)m]},$$

$$p = 1.0 - \frac{0.6097}{m} + \frac{0.05463}{m^2},$$

and $\Gamma(x) = \int_0^\infty t^{x-1} e^{-t} dt$ is the gamma function. The variable r_* is expressed by the elliptical radius, $r_*^2 = R^2 + z^2/q^2$ in cylindrical coordinates, so $\nu(r_*)$ is constant on spheroidal shells with intrinsic axial ratio q that is related to the projected axial ratio q' and an inclination angle for the stellar system i so that $q'^2 = \cos^2 i + q^2 \sin^2 i$, where $i = 90^\circ$ when a galaxy is edge-on and $i = 0^\circ$ for face-on. The intrinsic axial ratio can be derived from $q = \sqrt{q'^2 - \cos^2 i} / \sin i$, and thus the inclination angle is constrained by $(q'^2 - \cos^2 i)$ being positive.

3.2 Dark components

For the dark matter halo, we adopt a generalized Hernquist profile given by Hernquist (1990) and Zhao (1996), but here we consider the non-spherical dark matter haloes of dSphs

$$\rho(R, z) = \rho_0 \left(\frac{r}{b_{\text{halo}}}\right)^{-\gamma} \left[1 + \left(\frac{r}{b_{\text{halo}}}\right)^\alpha\right]^{-\frac{\beta-\gamma}{\alpha}}, \quad (8)$$

$$r^2 = R^2 + z^2/Q^2, \quad (9)$$

where the six parameters are the following: ρ_0 and b_{halo} are the scale density and radius, α is the sharpness parameter of the transition from the inner slope $-\gamma$ to the outer slope $-\beta$, and Q is a constant axial ratio of the dark matter halo. For $(\alpha, \beta, \gamma) = (1, 3, 1)$, we recover the NFW profile (Navarro et al. 1996, 1997) motivated

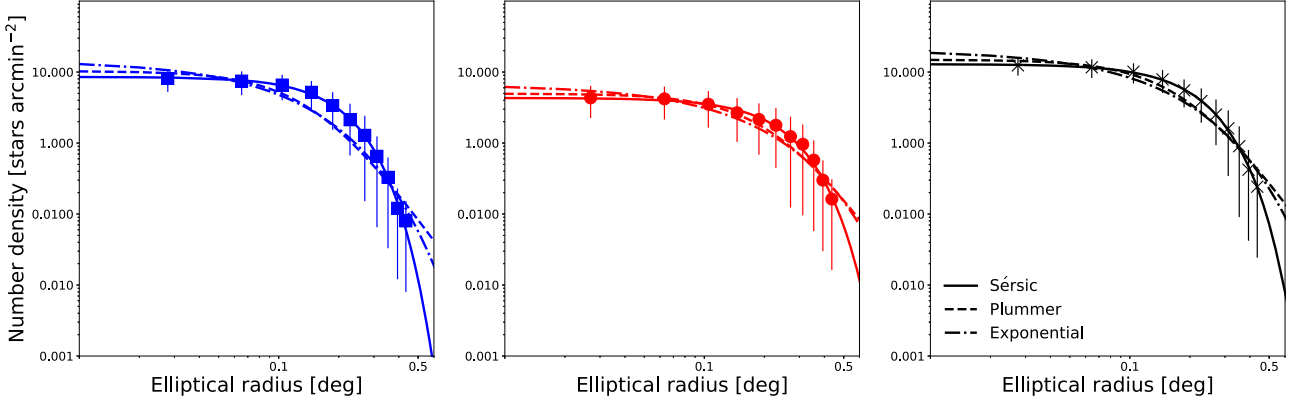


Figure 2. Radial density profiles of the intermediate (left-hand panel), old (middle panel), and all (right-hand panel) populations in Carina, respectively. The points with error bars in each panel denote the observed stellar density profiles from the photometric data. The solid, dashed, and dot-dashed lines are the best-fitting stellar profiles modelled by the Sérsic, Plummer, and the exponential profile, respectively.

Table 1. Parameter constraints for stellar surface density distributions of the two populations in Carina. The ‘ALL’ column indicates fitting results using all (INTERMEDIATE + OLD) stars in Carina.

	INTERMEDIATE	OLD	ALL
Sérsic profile			
Ellipticity	$0.29^{+0.02}_{-0.03}$	$0.32^{+0.04}_{-0.04}$	$0.33^{+0.02}_{-0.02}$
R_s [arcmin]	$11.7^{+0.7}_{-0.7}$	$14.3^{+1.4}_{-1.2}$	$12.5^{+0.9}_{-0.8}$
R_s [pc]	$357.4^{+21.4}_{-21.4}$	$436.8^{+36.7}_{-42.8}$	$381.8^{+27.5}_{-24.4}$
m	$0.50^{+0.04}$	$0.52^{+0.09}_{-0.02}$	$0.53^{+0.05}_{-0.03}$
reduced- χ^2	1.16	1.10	1.04
Plummer profile			
Ellipticity	$0.21^{+0.02}_{-0.02}$	$0.29^{+0.04}_{-0.04}$	$0.33^{+0.02}_{-0.02}$
R_p [arcmin]	$9.4^{+0.6}_{-0.9}$	$13.9^{+2.1}_{-2.7}$	$11.8^{+1.2}_{-0.6}$
R_p [pc]	$287.1^{+27.5}_{-18.3}$	$424.6^{+64.1}_{-45.8}$	$360.4^{+36.7}_{-18.3}$
reduced- χ^2	4.51	1.87	2.75
Exponential profile			
Ellipticity	$0.20^{+0.02}_{-0.02}$	$0.26^{+0.04}_{-0.04}$	$0.33^{+0.02}_{-0.02}$
R_e [arcmin]	$9.1^{+0.9}_{-0.6}$	$13.3^{+2.1}_{-1.5}$	$11.2^{+0.9}_{-0.6}$
R_e [pc]	$277.9^{+27.5}_{-18.3}$	$406.2^{+63.4}_{-45.8}$	$342.1^{+27.5}_{-18.3}$
reduced- χ^2	4.59	1.44	4.19

by cosmological pure dark matter simulations, while $(\alpha, \beta, \gamma) = (1.5, 3, 0)$ corresponds to the Burkert cored profile (Burkert 1995). Therefore, this dark matter halo model enables us to explore a wide range of physically plausible dark matter profiles.

An advantage of this assumed profile is that the form of equations (8) and (9) allows us to calculate the gravitational force in a straightforward way (van der Marel et al. 1994; Binney & Tremaine 2008). Using a new variable of integration $\tau \equiv a_0^2(1 - Q^2)[\sinh^2 u_m - ((1 - Q^2)^{-0.5} - 1)](a_0 = \text{const})$ in the spheroidal coordinate (u_m, v_m) , the gravitation force can be obtained by one-dimensional integration

$$\mathbf{g} = -\nabla\Phi = -\pi G Q a_0 \int_0^\infty d\tau \frac{\rho(\tilde{r}^2) \nabla \tilde{r}^2}{(\tau + a_0^2) \sqrt{\tau + Q^2 a_0^2}}, \quad (10)$$

where G is the gravitational constant, and \tilde{r}^2 is defined by

$$\frac{\tilde{r}^2}{a_0^2} = \frac{R^2}{\tau + a_0^2} + \frac{z^2}{\tau + Q^2 a_0^2}. \quad (11)$$

3.3 Axisymmetric Jeans analyses

Dwarf spheroidal galaxies are generally regarded as collisionless systems. The spatial and velocity distributions of stars in such a dynamical system are described by its phase-space DF. As the system is in dynamical equilibrium and collisionless under the smooth gravitational potential, the DF obeys the steady-state collisionless Boltzmann equation (Binney & Tremaine 2008). Since the families of solutions satisfied by this equation are innumerable, additional assumptions and simplifications are required. One of the classical and useful ways to alleviate this issue is to take the velocity moments of the DF. The equations derived from this approach are called Jeans equations. In what follows, we describe these equations for the cases of axisymmetric mass distributions. This is motivated by the fact that the luminous part of dSphs is not really spherically symmetric, nor are the shapes of dark matter haloes predicted by high-resolution Λ -dominated CDM simulations.

In the axisymmetric case, a specific but well-studied assumption is to suppose that the DF is of the form $f(E, L_z)$, where E and L_z denote the binding energy and the angular momentum component towards the symmetry axis, respectively. In this case, the mixed velocity moments vanish and the velocity dispersion $(\overline{v_R^2}, \overline{v_\phi^2}, \overline{v_z^2})$ in cylindrical coordinates (R, ϕ, z) obeys $\overline{v_R^2} = \overline{v_z^2}$ (Binney & Tremaine 2008; Hayashi & Chiba 2012), that is, a velocity anisotropy parameter β_z defined as $\beta_z = 1 - \overline{v_z^2}/\overline{v_R^2}$ is zero. However, β_z could be in general non-zero and is degenerated strongly with the dark-halo shape (Cappellari 2008; Hayashi & Chiba 2015b, H16), and thus non-zero β_z is essential to obtain more convincing results from axisymmetric mass models. In this work, we follow the approach of Cappellari (2008) who assumed that the velocity ellipsoid is aligned with the (R, ϕ, z) coordinate and the anisotropy is constant. We note that these assumptions are supported by dark matter simulations performed by Vera-Ciro et al. (2014). Using the velocity anisotropy, the second-order axisymmetric Jeans equations can be written as

$$\overline{v_z^2} = \frac{1}{v(R, z)} \int_z^\infty v \frac{\partial \Phi}{\partial z} dz, \quad (12)$$

$$\overline{v_\phi^2} = \frac{1}{1 - \beta_z} \left[\overline{v_z^2} + \frac{R}{v} \frac{\partial (v \overline{v_z^2})}{\partial R} \right] + R \frac{\partial \Phi}{\partial R}, \quad (13)$$

where ν is the three-dimensional stellar density and Φ is the gravitational potential dominated by dark matter. We also assume for simplicity that the density of the tracer stars has the same orientation and symmetry as that of the dark halo.

In order to compare second velocity moments from Jeans equations with those from the observations, we need to derive projected second velocity moments by integrating $\overline{v_z^2}$ and $\overline{v_\phi^2}$ along the line of sight. To do this, we follow the method given in Tempel & Tenjes (2006, see also Hayashi & Chiba 2012), which took into account the inclination of the galaxy with respect to the observer.

4 FITTING PROCEDURE

4.1 Likelihood function

We consider different stellar populations within the same gravitational potential originating from a dark halo, but each population shows a different spatial and velocity distribution. Therefore, we set the same likelihood function for each population and combine them to obtain tighter constraints on the dark halo parameters.

For each stellar population $k = \{\text{Int}, \text{Old}\}$ (where Int and Old mean intermediate- and old-age populations, respectively), we assume that the line-of-sight velocity distribution is Gaussian and centred on the systemic velocity of the galaxy $\langle u \rangle$. Given that the total number of member stars for each population is N^k , and the i th star has the measured line-of-sight velocity $u_i \pm \delta_{u,i}$ at the sky plane coordinates (x_i, y_i) , the likelihood function for each population k is constructed as

$$\mathcal{L}^k = \prod_{i=1}^{N^k} \frac{1}{(2\pi)^{1/2} \left[(\delta_{u,i}^k)^2 + (\sigma_i^k)^2 \right]^{1/2}} \exp \left[-\frac{1}{2} \frac{(u_i^k - \langle u^k \rangle)^2}{(\delta_{u,i}^k)^2 + (\sigma_i^k)^2} \right], \quad (14)$$

where σ_i^k is the theoretical line-of-sight velocity dispersions at (x_i, y_i) specified by model parameters (as described below) and derived from the Jeans equations. Then, combining the intermediate and old populations, we obtain the ‘joint’ likelihood function

$$\mathcal{L}_{\text{joint}} = \prod_k \mathcal{L}^k = \mathcal{L}^{\text{Int}} \times \mathcal{L}^{\text{Old}}. \quad (15)$$

We also perform the fitting analysis for the whole stellar sample using ‘single’ likelihood function, which means that we do not separate between the intermediate- and old-age stellar populations, to compare with the results from the joint likelihood function.

4.2 Model parameters

For the case of axisymmetric models, the model parameters are the six parameters of the dark halo and three parameters of the stellar properties in the axisymmetric case, for which we adopt the uniform/log-uniform priors. Here, we describe these parameters.

Since we assume that the different stellar populations move in the gravitational potential of a dark halo with the generalized Hernquist density profile, there are six free parameters of the dark halo profile: (1) the axial ratio of dark halo Q , (2) the scale radius b_{halo} , (3) the scale density ρ_0 , (4) the sharpness of the transition from the inner to the outer density slope α , (5) the outer density slope β , and (6) the inner density slope γ . For the stellar component, we consider different velocity anisotropy parameters, while we assume that the inclination of each stellar population is identical. Thus, there are three free parameters: (7) the velocity anisotropy for the

intermediate-age population $\beta_{z,\text{Int}}$, (8) that for old-age one $\beta_{z,\text{Old}}$, and (9) the inclination angle i . For this total of nine parameters, the prior ranges of each parameter are:

- (1) $0.1 \leq Q \leq 2.0$;
- (2) $0 \leq \log_{10}[b_{\text{halo}}/\text{pc}] \leq +5$;
- (3) $-5 \leq \log_{10}[\rho_0/(M_\odot \text{pc}^{-3})] \leq +5$;
- (4) $0.5 \leq \alpha \leq 3$;
- (5) $3 \leq \beta \leq 10$;
- (6) $0 \leq \gamma \leq 1.2$;
- (7) $-1 \leq -\log_{10}[1 - \beta_{z,\text{Int}}] < +1$;
- (8) $-1 \leq -\log_{10}[1 - \beta_{z,\text{Old}}] < +1$;
- (9) $\cos^{-1}(q') \leq i \leq 90^\circ$.

As we described in Section 3.1, the lower limit of the inclination angle i is confined by $q'^2 - \cos^2 i > 0$. Besides the above free parameters, the systemic velocity $\langle u^k \rangle$ of the system is also included as a free parameter with a flat prior. When we estimate these parameters using a single likelihood function, the number of free parameters is eight because we can then consider only one stellar velocity anisotropy parameter.

In order to explore the large parameter space efficiently, we adopt Markov Chain Monte Carlo (MCMC) techniques, based on Bayesian parameter inference, with the standard Metropolis–Hasting algorithm (Metropolis et al. 1953; Hastings 1970). We take several post-processing steps (burn-in step, the sampling step, and length of the chain) to generate independent samples that can avoid the influence of the initial conditions, and then we obtain the posterior probability distribution function (PDF) of the set of free parameters. By calculating the percentiles of these PDFs, we are able to compute credible intervals for each parameter in a straightforward way.

5 RESULTS

In this section, we present the results of the MCMC fitting analysis for two-stellar components in Carina with nine free parameters, and compute the median and credible interval values from the resulting PDF.

Fig. 3 displays the posterior PDFs derived from the MCMC procedure with a joint likelihood function (15). Relatively, the halo parameters b_{halo} and ρ_0 are better constrained than the other parameters. The PDFs for the inner slope of dark matter density, γ , are more widely spread than for the above two parameters, but still they indicate that the data show preference for shallower cuspy or cored dark matter density profile in Carina. On the other hand, (Q, α, β, i) are so widely distributed in these parameter spaces that it is difficult to confine the parameter distributions of these. In particular, the axis ratio of the dark halo has a strong degeneracy with the stellar velocity anisotropy, β_z . As discussed in several papers (Cappellari 2008; Battaglia, Helmi & Breddels 2013, and HC15), the change of these has a similar effect on the profiles of the line-of-sight velocity dispersions. In addition, there also exists a degeneracy between β_z for the intermediate- and the old stellar population, even though both parameters have the peak of PDF at $-\log_{10}[1 - \beta_z] \sim 0.4$ which means that the stellar velocity distributions for both populations in Carina are similar and are likely to possess velocity dispersion more strongly biased in the R direction than in the z direction.

To confirm whether our unbinned analysis can reproduce the observed kinematics of Carina, we calculate profiles of the line-of-sight velocity dispersions for both populations using fitting param-

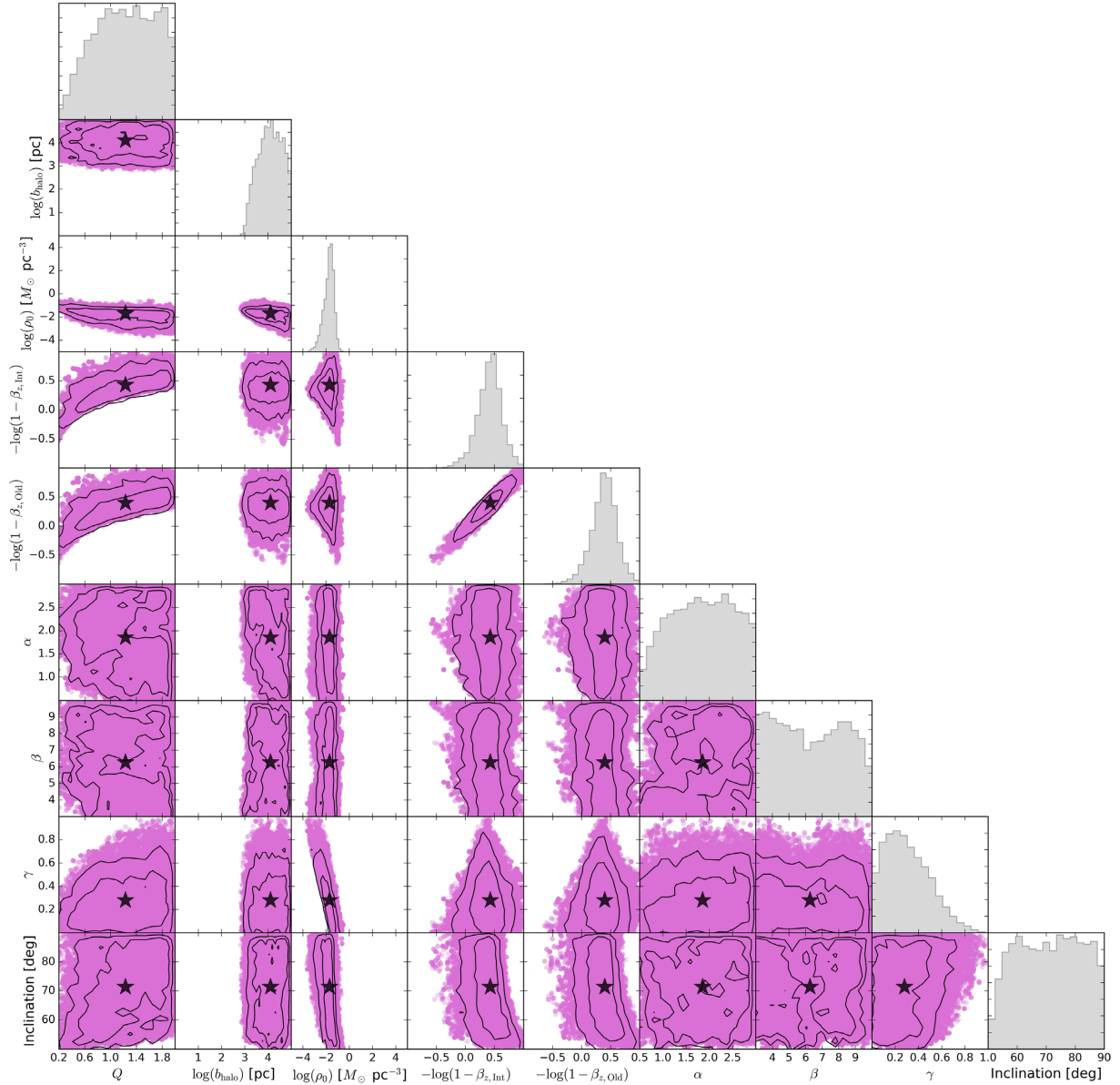


Figure 3. Posterior distributions for the fitting parameters calculated from the joint likelihood analysis. The star in each panel denotes the median value of each parameter. The black lines represent the 1σ and 2σ regions. For some parameters, especially α and β , the distributions are not well constrained.

eters in our models and the observational data. To estimate these profiles from the models, we obtain the output parameters of their MCMC chains, and then we compute the line-of-sight velocity dispersion profiles through the axisymmetric Jeans equations for all cases of the output parameter sets. Finally, we calculate median, 15.87th and 84.13th percentiles (i.e. 68 per cent confidence level), and 2.28th and 97.72nd percentiles (i.e. 95 per cent confidence level) of them from all parameter sets. On the other hand, in order to obtain these binned profiles from the observed line-of-sight velocity data, we adopt the common way of using binning profiles. First, assuming an axisymmetric stellar distribution adopted in this work, the projected positions (x, y) of the line-of-sight velocity data are folded into the first quadrant. Secondly, we transform the projected stellar distribution in the first quadrant to two-dimensional polar coordinates (r, θ), where $\theta = 0^\circ$ is set along the major axis of the stellar distribution, and then divide this into three areas: $\theta = 0^\circ - 30^\circ$, $30^\circ - 60^\circ$, and $60^\circ - 90^\circ$, respectively. For convenience,

the first azimuthal region ($\theta = 0^\circ$ and 30°) is referred to as a major axis, the second one as a middle axis, and third one as a minor axis. Finally, for each area, we radially divide stars into bins so that a nearly equal number of stars is contained in each bin. Fig. 4 shows this quantity along the projected major, minor, and middle axis for the intermediate- and old stellar populations in Carina. The dashed line and the shaded region in each panel denote the median value and confidence levels (light: 68 per cent, dark: 95 per cent) of the resultant unbinned MCMC analysis of the model profiles, whereas the points with error bars are binned second velocity moments calculated from the observed data with the above method. As shown in this figure, the profiles calculated from the results of our MCMC analysis are in good agreement with binned profiles along each axis, even though we do not perform any binned fitting analysis. Furthermore, it is found that all second moment curves are almost flat, irrespective of the stellar population and the axis direction. These flat profiles are similar to those found in previous works even

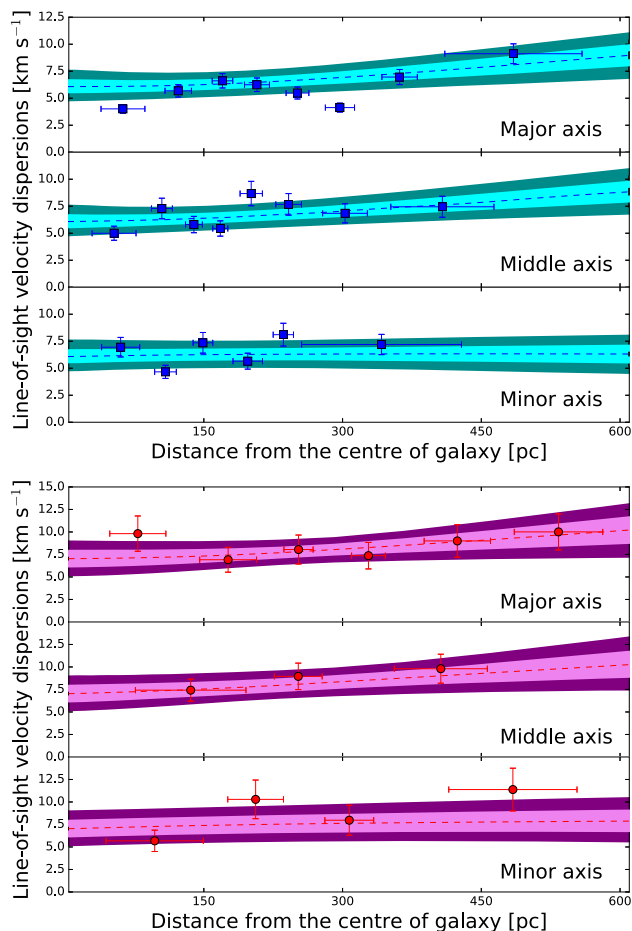


Figure 4. Profiles of the line-of-sight velocity dispersions along the major (first row), middle (second row), and minor (third row) axis for the intermediate- (top panel) and old-age (bottom panel) population. The colour points with error bars in each panel denote observed velocity dispersions. The dashed lines are median values of the models and the light and dark shaded regions encompass the 68 per cent and 95 per cent confidence levels from the results of the unbinned MCMC analysis. The methods for generating the binned profiles are described in the main text.

assuming spherically symmetric stellar distributions (Walker et al. 2009).

Table 2 tabulates the results of MCMC fitting for the joint (first row) and the single (second row) likelihood analysis.² We show the median and 1σ (68 per cent) confidence intervals of the free parameters, which correspond to the 50th (median), 16th (lower error), and 84th (upper error) percentiles of the posterior PDFs, respectively. β_{ALL} denotes the velocity anisotropy for all stars, and

²In addition, we perform the MCMC fitting for spherical mass models to compare with our axisymmetric mass models. For the spherical mass models here, we assume two cases of models: one with the axial ratios of both dark (Q) and luminous (q') components equal to unity, and another such that the dark halo is assumed to be spherical ($Q = 1$), but the stellar distributions are not spherical ($q' \neq 1$). Then, using the results of the MCMC fitting, we estimate a Bayes factor which is the ratio of the mean posterior distribution of the axisymmetric to spherical symmetric mass models. The resulting Bayes factor in the case of ($Q = 1, q' = 1$) is 450.9, and that in the case of ($Q = 1, q' \neq 1$) is 37.8, respectively. It is clearly found that our axisymmetric mass models yield a relatively better fit than any spherical ones.

thus this fitting result is shown only in the second row. Comparing the results of the joint and the single likelihood analysis, we find that there is no significant difference in both the median and the confidence intervals for all parameters. This is because in the joint analysis the number of stars is probably not large enough to obtain stronger limits on the dark halo parameters than in the case of the single analysis. In order to set constraints on the dark halo more robustly, the number of observed stars in the kinematic sample is absolutely essential. Nevertheless, the joint analysis enables us to investigate velocity anisotropy profiles separately for each of the components (see Section 6.3).

6 DISCUSSION

6.1 Astrophysics factors for Carina

The Galactic dSph galaxies are ideal targets for constraining particle candidates for dark matter through indirect searches utilizing γ -rays or X-rays originating from dark matter annihilations and decays. This is because these galaxies possess large dark matter content, are located at relative proximity, and have low astrophysical foregrounds of γ -rays and X-rays. The γ -ray and X-ray flux can be derived by the annihilation cross-section or decay rate which estimates how dark matter particles transform into standard model particles (the so-called particle physics factor) and line-of-sight integrals over the dark matter distribution within the system (the so-called astrophysics factor). In particular, the astrophysics factor depends largely on the annihilation and decay fluxes. Therefore, in order to obtain robust limits on particle candidates for dark matter, accurate understanding of the dark matter distribution in dSphs is of crucial importance. So far, some previous works have already evaluated the astrophysics factors for Carina dSph assuming spherical distribution (Ackermann et al. 2014; Bonnivard et al. 2015; Geringer-Sameth et al. 2015) and axisymmetric distribution (H16, Klop et al. 2017) of dark matter density. However, here we calculate for the first time the astrophysics factors for Carina using the fitting results from the joint likelihood analysis of multiple stellar components and assuming more general dark halo models that include non-sphericity and the generalized Hernquist density profile. In this section, we estimate the astrophysics factors from our results and compare them with those from previous studies. To do this adequately, we use only the factors integrated within a fixed integration angle 0.5° .

The astrophysics factors for dark matter annihilation and decay are given by

$$J = \int_{\Delta\Omega} \int_{los} d\ell d\Omega \rho^2(\ell, \Omega) \quad [\text{annihilation}], \quad (16)$$

$$D = \int_{\Delta\Omega} \int_{los} d\ell d\Omega \rho(\ell, \Omega) \quad [\text{decay}], \quad (17)$$

which are called J factor and D factor (Gunn et al. 1978; Bergström, Ullio & Buckley 1998). These factors correspond to the line-of-sight integral of the square of dark matter density for annihilation and the dark matter density for decay, respectively, within the solid angle $\Delta\Omega$. To estimate these factors for axisymmetric dark matter distributions, the output parameters ($Q, b_{\text{halo}}, \rho_0, \alpha, \beta, \gamma, i$) from their MCMC chains are used to calculate the dark matter annihilation J -factor and decaying dark matter D -factor integrated within 0.5° solid angle using equations (16) and (17). We also calculate the median and 1σ uncertainties of J - and D -factors using the marginalized

Table 2. Parameter constraints with Joint and Single likelihood functions. Errors correspond to the 1σ range from our analysis.

Parameters	Q	$\log_{10}(b_{\text{halo}})$ [pc]	$\log_{10}(\rho_0)$ [$M_{\odot} \text{pc}^{-3}$]	α	β	γ	$-\log_{10}$ [$1 - \beta_z, \text{ALL}$]	$-\log_{10}$ [$1 - \beta_z, \text{Inl}$]	$-\log_{10}$ [$1 - \beta_z, \text{Otd}$]	i [deg]
Joint	$1.23^{+0.51}_{-0.52}$	$4.11^{+0.55}_{-0.58}$	$-1.70^{+0.34}_{-0.52}$	$1.85^{+0.74}_{-0.77}$	$6.27^{+2.42}_{-2.35}$	$0.28^{+0.23}_{-0.17}$	—	$0.43^{+0.18}_{-0.22}$	$0.40^{+0.19}_{-0.22}$	$71.35^{+12.28}_{-12.66}$
Single	$1.34^{+0.42}_{-0.55}$	$4.21^{+0.54}_{-0.61}$	$-1.69^{+0.26}_{-0.42}$	$2.24^{+0.52}_{-0.67}$	$6.68^{+2.20}_{-2.40}$	$0.21^{+0.19}_{-0.14}$	$0.46^{+0.18}_{-0.23}$	—	—	$72.89^{+10.89}_{-13.38}$

Table 3. Comparison of J and D values integrated within 0.5° calculated from this work and taken from the previous works. The values of error correspond 1σ uncertainties. The units of $J_{0.5}$ and $D_{0.5}$ are [$\text{GeV}^2 \text{cm}^{-5}$] and [GeV cm^{-2}], respectively.

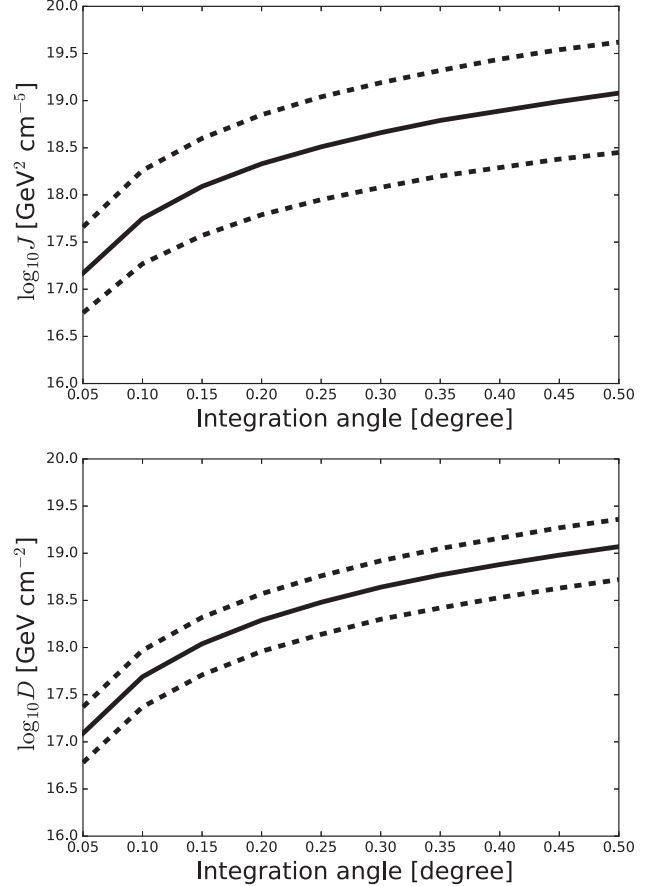
DM Models	This work	Hayashi et al. (2016, H16)	Geringer-Sameth et al. (2015)
	Axisymmetric	Axisymmetric	Spherical
$\log_{10}J_{0.5}$	$19.08^{+0.54}_{-0.63}$	$17.97^{+0.46}_{-0.28}$	$17.87^{+0.10}_{-0.09}$
$\log_{10}D_{0.5}$	$19.07^{+0.29}_{-0.63}$	$18.19^{+0.26}_{-0.25}$	$17.90^{+0.17}_{-0.16}$

PDFs of these factors. The methods are described in more detail in section 2 of H16.

Table 3 shows a comparison of the J and D values integrated within 0.5° solid angle of our results with those of previous works. It is clear from this table that there are differences in the median values and the uncertainties of the J - and D -factor between our estimates and other studies. The reasons for these differences are not only the effects of non-sphericity but also the size of the kinematic data sample and the number of free parameters in the assumed dark matter density profile. Since H16 have already discussed the differences in the astrophysics factors between their axisymmetric mass models and the spherical ones from Geringer-Sameth et al. (2015), in what follows we focus on the differences between axisymmetric models in this work and in H16.

Naturally, the main reason why the J and D uncertainties from this work are larger than those from H16 would be the difference in the number of fitting parameters of dark halo profiles. H16 assumed that the outer slope of dark matter profiles is $\rho \propto r^{-3}$ consistently and the parameter of the transition from the inner to the outer density slope has a constant value, so that the total number of dark halo parameters was four. On the other hand, the dark matter profile we adopt here is a generalized Hernquist profile that takes into account the outer slope and the curvature of the density profile as free parameters, and thus we have six parameters for the dark halo in total. As for the difference in the median values, it can be understood by the fitting results for the scale length (b_{halo}) and the scale density (ρ_0) of the dark halo profile. While H16 obtained $\log_{10}(b_{\text{halo}}/[\text{pc}]) = 3.5^{+0.7}_{-0.6}$ and $\log_{10}(\rho_0/[M_{\odot}\text{pc}^{-3}]) = -2.2^{+1.0}_{-0.9}$ from their MCMC fitting procedure, our fitting result from the joint likelihood analysis gives $\log_{10}(b_{\text{halo}}/[\text{pc}]) = 4.1^{+0.6}_{-0.5}$ and $\log_{10}(\rho_0/[M_{\odot}\text{pc}^{-3}]) = -1.7^{+0.3}_{-0.5}$. Therefore, the value of the scale length (the scale density) estimated from our results is about a factor of 4 (3) larger than that from H16, and thus the J and D factors in this study should be higher than the values in the previous axisymmetric work. The reason for the difference in these dark halo parameters could be the different data volume of the stellar kinematic sample. The number of available velocity data for Carina was 776 stars in previous works, whereas this work utilizes 1389 stars to obtain limits on dark matter distribution. Thus, it is not surprising that fitting results in this work are not consistent with those in the others.

Furthermore, we find that our evaluated J - and D -factors for Carina have higher values in comparison with those for the other Milky Way dwarf satellites. Several known Galactic dwarf galaxies

**Figure 5.** Expected emission profiles for annihilation (top panel) and decay (bottom panel). The solid line in each panel denotes the median profile, and the dashed line corresponds to the $\pm 1\sigma$ distribution.

such as Draco, Ursa Minor, Coma Berenices, and Ursa Major II possess large mean J - and D -factors (e.g. Ackermann et al. 2015; Geringer-Sameth et al. 2015, H16). For instance, Draco, which might have the highest J and D value among classical dwarfs, has $\log_{10} J = 19.09^{+0.39}_{-0.36} \text{ GeV}^2 \text{cm}^{-5}$ and $\log_{10} D = 18.84^{+0.23}_{-0.21} \text{ GeV cm}^{-2}$ as given by H16. We therefore suggest that the Carina dSph becomes one of the most promising detectable target among the classical dwarf galaxies for an indirect search of dark matter annihilation and decay.

Finally, to facilitate the evaluation of a survey design using γ -ray or X-ray observation for Carina, we quantify the spatial extent of the emission from dark matter annihilation and decay. The angular distributions of emission can provide useful information about how large areas are required in optimal observations. Moreover, the detection of a spatially varying annihilation or decay emission signal is directly linked to the possibility of revealing the nature of the dark matter halo. Fig. 5 displays the median value and 1σ confidence intervals of the J - and D -factor as a function of the integration solid

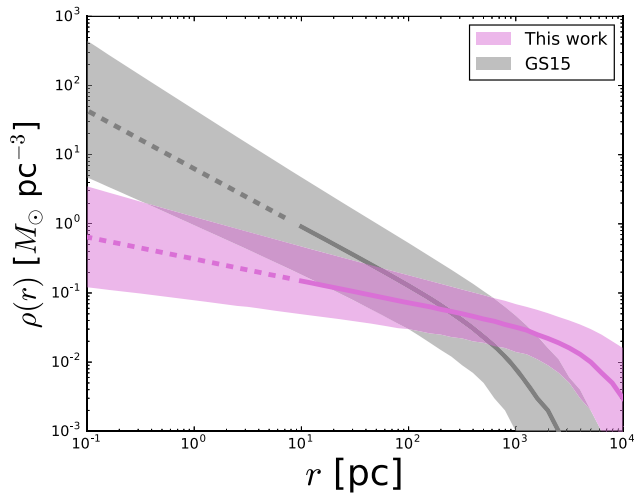


Figure 6. Derived dark matter density profile from our Jeans analysis (purple) and the results of **GS15** (grey). The dashed lines denote smaller radii than the positions of the innermost observed member stars, so the density profile within the region is less certain. On the other hand, the solid lines represent the reliable density profiles. The shaded regions denote $\pm 1\sigma$ intervals.

angle. We calculate astrophysical factors extended to 0.5° integration angle, because the outermost observed member star in Carina is located about 0.5° from the centre of the galaxy. From this figure, we find that beyond the integration angle $\sim 0.1^\circ$, the J and D values increase moderately, thereby suggesting that to preform the optimal γ -ray or X-ray observation of Carina, the observational area larger than 0.1° would be required.

6.2 Dark matter density profile

Using the fitting results for dark matter density parameters, we present the inferred dark matter density profile of Carina. In addition, we also calculate the density profile given by Geringer-Sameth et al. (2015, hereafter **GS15**) for comparison. Both dark halo profiles were modelled with the same free parameters, except for the difference in non-sphericity and thus we can compare between their density profiles reliably.

Fig. 6 shows the dark matter density profile estimated from our joint analysis (purple) and from **GS15** (grey). For our results, we compute the dark matter density profile along its major axis. On the other hand, for **GS15**, we calculate the density profile using the median and $\pm 1\sigma$ values of dark halo parameters listed in table 4 of their paper. We find from this figure that although the density distribution in the inner region is not a robust result and has large uncertainties, the inner density slope from this work favours shallower values than that from **GS15**. Moreover, our estimated dark halo size, which corresponds to the radius of the transition from the inner to the outer slope, is larger than that from the previous spherical work. This means that in our case the dark matter would be more widely distributed, thereby implying that the astrophysics factors can have large values even though the preferred inner dark matter density is shallower.

6.3 Velocity anisotropy

In general, axisymmetric models are to some extent capable of taking into account the velocity anisotropy that depends on the

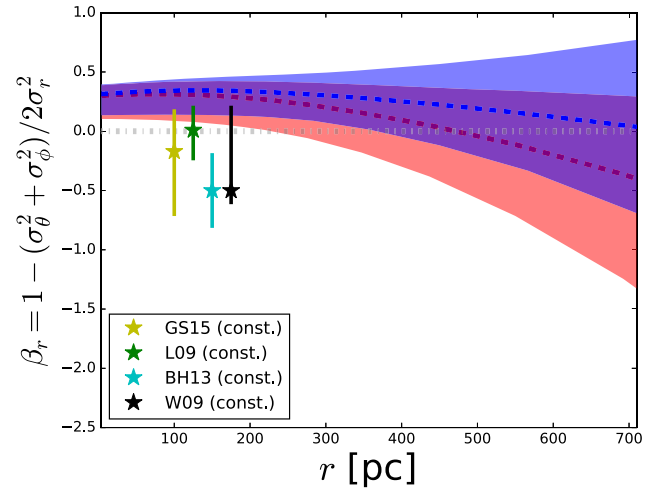


Figure 7. The profiles of the velocity anisotropy β_r for the intermediate- (blue) and old-age (red) stellar populations. The dashed lines and shaded regions denote the median values and the $\pm 1\sigma$ intervals, respectively. The grey dash-dotted line corresponds to the isotropic value, i.e. $\beta_r = 0$. The coloured stars with error bars are the constant velocity anisotropy values given by Walker et al. (2009, black star), Łokas (2009, green), Breddels & Helmi (2013, cyan), and Geringer-Sameth et al. (2015, yellow), respectively.

spatial coordinates. This is important because revealing the stellar velocity anisotropy provides critical information to understand the dynamical evolution history and the dark matter distribution in the system. In order to compare with previous results, we transform the second velocity moments in cylindrical coordinates to spherical coordinates and estimate the stellar velocity anisotropy in a spherical model which is given by

$$\beta_r = 1 - \frac{\sigma_\theta^2 + \sigma_\phi^2}{2\sigma_r^2}, \quad (18)$$

where $\sigma_\theta^2 = \overline{v_\theta^2}$, $\sigma_\phi^2 = \overline{v_\phi^2} - \overline{v_\phi}^2$, and $\sigma_r^2 = \overline{v_r^2}$ in spherical coordinates (r, θ, ϕ) . Fig. 7 displays the velocity anisotropy profiles calculated from our axisymmetric models for intermediate- (blue) and old-age (red) stellar populations. The dashed lines denote median values of the quantity, and the shaded regions correspond to their 1σ confidence intervals. If a galaxy has an isotropic velocity ellipsoid for stars, β_r is equal to zero. We find from this figure that the common assumptions of anisotropy constant with radius or equal to zero would be unrealistic. Moreover, both populations are radially anisotropic at small radii. Then, the velocity anisotropy of the intermediate population decreases gradually to isotropic with increasing radius, while that of old one becomes moderately tangentially anisotropic outwards, even though there are large uncertainties especially in outer parts of the system.

Fig. 7 also shows the values of the constant-velocity anisotropy estimated by previous works assuming spherical symmetry taken from Walker et al. (2009, black star), Łokas (2009, green), Breddels & Helmi (2013, cyan), and Geringer-Sameth et al. (2015, yellow), respectively. We note that these values of velocity anisotropy do not depend on the radius (i.e. x -axis in this figure), since these are ‘constant’ values of β_r . Walker et al. (2009) used single-component spherical Jeans equations to model line-of-sight velocity dispersions of the classical dSphs, and they found that Carina dSph favours a mild tangential velocity bias for any dark halo mass profiles assumed. Łokas (2009) also solved spherical Jeans equations to reproduce the projected higher order velocity moment (kurtosis) as

well as second moment, and showed that an almost isotropic stellar velocity distribution is preferred ($\beta_r \sim 0.01$). Geringer-Sameth et al. (2015) performed dynamical analysis similar to Walker et al. (2009), with a difference in the assumed dark halo profiles and likelihood functions. They found slightly tangentially biased velocity anisotropy. On the other hand, Breddels & Helmi (2013) implemented single-component orbit-based Schwarzschild models and computed line-of-sight velocity dispersions and kurtoses of the luminous dSphs. From their analysis, the velocity anisotropy of Carina is clearly tangential.

Broadly, the velocity anisotropy profiles calculated from our analysis are consistent with the single-component analyses from the previous works in the outer parts. However, our axisymmetric models assume a constant β_z for simplicity and thereby our calculated β_r is strongly limited. In order to investigate the detailed profile of the velocity anisotropy, we need more realistic dynamical models for dSphs, relaxing the assumption of a constant β_z and more stellar kinematic data in the future.

The feature that each population has more tangential (less radial) velocity anisotropy at larger radii, implies a vestige of tidal disturbances in the dynamical evolution of the stellar system, which can be quite strong for dwarfs on eccentric orbits in an external gravitational potential (Baumgardt & Makino 2003; Read et al. 2006). In particular, the old-age population of Carina is widely extended and thus is more likely to be tangentially biased by tidal effects. Furthermore, Łokas et al. (2010) considered a scenario where a dSph could have originated from disk dwarf galaxy whose disc was transformed into a bar-like structure and tidally stripped by the effects of the Galactic gravitational potential. In this scheme, the velocity anisotropy profile of the bar-like structure is radially biased in the inner part, while in the outskirts the tidal effects would dominate so that the profile should decrease towards tangentially biased. This prediction is in very good agreement with the velocity anisotropy profile of Carina found here as well as its velocity structure measured by Fabrizio et al. (2016) which included the detection of remnant rotation in the dwarf. In addition, using photometric observations Battaglia et al. (2012) found evidence for the presence of tidal tails and isophote twists in Carina, which also provide observational evidence in favour of tidal interactions. In spite of large uncertainties in our estimated velocity anisotropy, our results seem to catch a glimpse of kinematical features due to tidal effects from the Galactic potential.

7 CONCLUDING REMARKS

In this work, based on axisymmetric Jeans equations, we constructed non-spherical dynamical models taking into account multiple components within a stellar system. We assumed that these multiple stellar populations with different dynamical properties settle in the same gravitational potential provided by a dark halo. We used a joint likelihood function that is a combination of likelihood functions for each population but assumed the same dark halo parameters. Applying this dynamical modelling technique to the Carina dSph galaxy whose stellar populations can be separated by the photometric colour–magnitude diagram, we found several interesting results concerning the dark halo and kinematic properties of Carina.

First, in our joint analysis, the halo parameters b_{halo} and ρ_0 are better constrained than the other parameters. In comparison with previous works, both parameters in our results have significantly higher values. For the inner slope of dark matter density, although the uncertainties of this parameter are still large, we have found

that for the Carina dark halo a shallow cusped or cored dark matter profile is preferred. On the other hand, (Q, α, β, i) are very widely distributed in the parameter spaces, and it is difficult to constrain these parameter distributions, even in joint analysis. We believe that for the joint analysis to work better and give stronger limits on the dark halo parameters a larger number of observed stars in the kinematic sample is absolutely essential. Still, the joint analysis enables us to investigate velocity anisotropy profiles separately for each of the populations.

Secondly, using our fitting results, we have estimated astrophysics factors for dark matter annihilation and decay. We found that these factors for Carina have the highest values among those of classical dSphs thereby suggesting that this galaxy is one of the most promising detectable targets among the classical dwarf galaxies for an indirect search with γ -ray and X-ray observations. We have also calculated stellar velocity anisotropy profiles for intermediate- and old-age populations and found that both are radially anisotropic in the inner region, while the former is approaching isotropy and the latter becomes mildly tangentially biased in the outer regions. Although these estimates of velocity anisotropy are still subject to large uncertainties, this feature provides us with the observational kinematic evidence of tidal effects from the Galactic potential.

So far, the dark matter density profile of the Carina dSph galaxy still has large uncertainties because the dark halo parameters, especially Q , β_z , and i , are not strongly constrained. To improve these estimates, we require not only a considerable amount of photometric and spectroscopic data but also proper motions of the member stars within the galaxy. In particular, the only way to break the degeneracy between the shapes of the dark halo and the stellar velocity anisotropy is still to measure three-dimensional velocities of stars. Further observational progress implementing space and ground-based telescopes will enable us to measure a huge number of stellar kinematic and metallicity data and, in the more remote future, provide phase-space information for stellar systems, thereby allowing us to set more robust constraints on the dark matter density profile in dSphs.

ACKNOWLEDGEMENTS

We are grateful to the referee for her/his careful reading of our paper and thoughtful comments. This work was supported in part by the MEXT Grant-in-Aid for Scientific Research on Innovative Areas, No. 16H01090, No. 18H04359, and No. 18J00277 (for KH), by the Polish National Science Centre under grant 2013/10/A/ST9/00023 (for EŁŁ), and by grant AYA2014-56795-P of the Spanish Ministry of economy and Competitiveness (for MM).

REFERENCES

- Ackermann M. et al., 2014, *Phys. Rev. D*, 89, 042001
 Ackermann M., Albert A., Anderson B. et al., 2015, *Phys. Rev. Lett.*, 115, 231301
 Agnello A., Evans N. W., 2012, *ApJ*, 754, L39
 Amorisco N. C., Evans N. W., 2012, *MNRAS*, 419, 184
 Amorisco N. C., Agnello A., Evans N. W., 2013, *MNRAS*, 429, L89
 Anderhalden D., Schneider A., Macciò A. V., Diemand J., Bertone G., 2013, *J. Cosmo. Astropart. Phys.*, 3, 014
 Battaglia G. et al., 2006, *A&A*, 459, 423
 Battaglia G., Helmi A., Tolstoy E., Irwin M., Hill V., Jablonka P., 2008, *ApJ*, 681, L13
 Battaglia G., Tolstoy E., Helmi A., Irwin M., Parisi P., Hill V., Jablonka P., 2011, *MNRAS*, 411, 1013

- Battaglia G., Irwin M., Tolstoy E., de Boer T., Mateo M., 2012, *ApJ*, 761, L31
- Battaglia G., Helmi A., Breddels M., 2013, *New Astron. Rev.*, 57, 52
- Baumgardt H., Makino J., 2003, *MNRAS*, 340, 227
- Bergström L., Ullio P., Buckley J. H., 1998, *Astropart. Phys.*, 9, 137
- Binney J., Tremaine S., 2008, *Galactic Dynamics*. Princeton Univ. Press, Princeton, NJ
- Bonnivard V. et al., 2015b, *MNRAS*, 453, 849
- Bono G. et al., 2010, *PASP*, 122, 651
- Boyarsky A., Neronov A., Ruchayskiy O., Tkachev I., 2010, *Phys. Rev. Lett.*, 104, 191301
- Bozek B., Boylan-Kolchin M., Horiuchi S., Garrison-Kimmel S., Abazajian K., Bullock J. S., 2016, *MNRAS*, 459, 1489
- Breddels M. A., Helmi A., 2013, *A&A*, 558, A35
- Breddels M. A., Helmi A., 2014, *ApJ*, 791, L3
- Burkert A., 1995, *ApJ*, 447, L25
- Cappellari M., 2008, *MNRAS*, 390, 71
- Coppola G. et al., 2013, *ApJ*, 775, 6
- Dall’Ora M. et al., 2003, *AJ*, 126, 197
- Di Cintio A., Brook C. B., Dutton A. A., Macciò A. V., Stinson G. S., Knebe A., 2014a, *MNRAS*, 441, 2986
- Di Cintio A., Brook C. B., Macciò A. V., Stinson G. S., Knebe A., Dutton A. A., Wadsley J., 2014b, *MNRAS*, 437, 415
- Elbert O. D., Bullock J. S., Garrison-Kimmel S., Rocha M., Oñorbe J., Peter A. H. G., 2015, *MNRAS*, 453, 29
- Evans N. W., An J., Walker M. G., 2009, *MNRAS*, 393, L50
- Fabrizio M. et al., 2011, *PASP*, 123, 384
- Fabrizio M. et al., 2012, *PASP*, 124, 519
- Fabrizio M. et al., 2015, *A&A*, 580, A18
- Fabrizio M. et al., 2016, *ApJ*, 830, 126
- Fiorentino G. et al., 2017, preprint ([arXiv:1712.04222](https://arxiv.org/abs/1712.04222))
- Gaia Collaboration, 2016, *A&A*, 595, A1
- Gaia Collaboration, 2018a, *A&A*, 616, A1
- Gaia Collaboration, 2018b, *A&A*, 616, A12
- Genina A. et al., 2018, *MNRAS*, 474, 1398
- Geringer-Sameth A., Koushiappas S. M., Walker M., 2015, *ApJ*, 801, 74
- Gilmore G., Wilkinson M. I., Wyse R. F. G., Kleyna J. T., Koch A., Evans N. W., Grebel E. K., 2007, *ApJ*, 663, 948
- Governato F. et al., 2012, *MNRAS*, 422, 1231
- Gunn J. E., Lee B. W., Lerche I., Schramm D. N., Steigman G., 1978, *ApJ*, 223, 1015
- Hastings W. K., 1970, *Biometrika*, 57, 97
- Hayashi K., Chiba M., 2012, *ApJ*, 755, 145
- Hayashi K., Chiba M., 2015, *ApJ*, 803, 11
- Hayashi K., Chiba M., 2015, *ApJ*, 810, 22
- Hayashi K., Ichikawa K., Matsumoto S., Ibe M., Ishigaki M. N., Sugai H., 2016, *MNRAS*, 461, 2914
- Hayashi K., Ishiyama T., Ogiya G., Chiba M., Inoue S., Mori M., 2017, *ApJ*, 843, 97
- Hernquist L., 1990, *ApJ*, 356, 359
- Herriot G. et al., 2014, in Marchetti E., Close L. M., Véran J.-P., eds, *Proc. SPIE Conf. Ser.* Vol. 9148. Adaptive Optics Systems IV. SPIE, Bellingham, p. 941810
- Irwin M., Hatzidimitriou D., 1995, *MNRAS*, 277, 1354
- Klop N., Zandanel F., Hayashi K., Ando S., 2017, *Phys. Rev. D*, 95, 123012
- Kormendy J., Freeman K. C., 2016, *ApJ*, 817, 84
- Kowalczyk K., Łokas E. L., Kazantzidis S., Mayer L., 2013, *MNRAS*, 431, 2796
- Lake G., 1990, *Nature*, 346, 39
- Lima Neto G. B., Gerbal D., Márquez I., 1999, *MNRAS*, 309, 481
- Łokas E. L., 2009, *MNRAS*, 394, L102
- Łokas E. L., Kazantzidis S., Klimentowski J., Mayer L., Callegari S., 2010, *ApJ*, 708, 1032
- Madau P., Shen S., Governato F., 2014, *ApJ*, 789, L17
- Massari D., Breddels M. A., Helmi A., Posti L., Brown A. G. A., Tolstoy E., 2018, *Nature Astron.*, 2, 156
- McConnachie A. W., 2012, *AJ*, 144, 4
- Metropolis N., Rosenbluth A. W., Rosenbluth M. N., Teller A. H., Teller E., 1953, *J. Chem. Phys.*, 21, 1087
- Monelli M. et al., 2003, *AJ*, 126, 218
- Monelli M. et al., 2013, *MNRAS*, 431, 2126
- Monelli M. et al., 2014, *ApJ*, 796, 90
- Navarro J. F., Frenk C. S., White S. D. M., 1996, *ApJ*, 462, 563
- Navarro J. F., Frenk C. S., White S. D. M., 1997, *ApJ*, 490, 493
- Ogiya G., Mori M., 2014, *ApJ*, 793, 46
- Oñorbe J., Boylan-Kolchin M., Bullock J. S., Hopkins P. F., Kereš D., Faucher-Giguère C. A., Quataert E., Murray N., 2015, *MNRAS*, 454, 2092
- Plummer H. C., 1911, *MNRAS*, 71, 460
- Read J. I., Wilkinson M. I., Evans N. W., Gilmore G., Kleyna J. T., 2006, *MNRAS*, 366, 429
- Salucci P., Burkert A., 2000, *ApJ*, 537, L9
- Salucci P., Wilkinson M. I., Walker M. G., Gilmore G. F., Grebel E. K., Koch A., Frigerio Martins C., Wyse R. F. G., 2012, *MNRAS*, 420, 2034
- Sérsic J. L., 1968, *Atlas de Galaxias Australes*. Observatorio Astronomico, Cordoba, Argentina
- Spergel D. N., Steinhardt P. J., 2000, *Phys. Rev. Lett.*, 84, 3760
- Spergel D. et al., 2015, preprint ([arXiv:1503.03757](https://arxiv.org/abs/1503.03757))
- Strigari L. E., Bullock J. S., Kaplinghat M., Simon J. D., Geha M., Willman B., Walker M. G., 2008, *Nature*, 454, 1096
- Strigari L. E., Frenk C. S., White S. D. M., 2017, *ApJ*, 838, 123
- Tempel E., Tenjes P., 2006, *MNRAS*, 371, 1269
- Tolstoy E. et al., 2004, *ApJ*, 617, L119
- van der Marel R. P., Evans N. W., Rix H.-W., White S. D. M., de Zeeuw T., 1994, *MNRAS*, 271, 99
- Vera-Ciro C. A., Sales L. V., Helmi A., Navarro J. F., 2014, *MNRAS*, 439, 2863
- Vogelsberger M., Zavala J., Loeb A., 2012, *MNRAS*, 423, 3740
- Walker M., 2013, in Oswald T. D., Gilmore G., eds, *Planets, Stars and Stellar Systems*. Vol. 5, Galactic Structure and Stellar Populations. Springer-Verlag, Berlin, p. 1039
- Walker M. G., Peñarrubia J., 2011, *ApJ*, 742, 20
- Walker M. G., Mateo M., Olszewski E. W., Peñarrubia J., Evans N. W., Gilmore G., 2009, *ApJ*, 704, 1274
- Watkins L. L., van de Ven G., den Brok M., van den Bosch R. C. E., 2013, *MNRAS*, 436, 2598
- Zhao H., 1996, *MNRAS*, 278, 488
- Zhu L., van de Ven G., Watkins L. L., Posti L., 2016, *MNRAS*, 463, 1117

This paper has been typeset from a $\text{\TeX}/\text{\LaTeX}$ file prepared by the author.